ADVANCED MATERIALS INTERFACES
www.advmatinterfaces.de

Check for updates

Laser-induced Modifiable Dual-wavelength Emissions from Lead Halide Perovskite Alloy Microcrystal

Yu Wu, Xia Shen, Qihang Lv, Qian Yang, Da Liu, Zhaohui Shan, Pengfei Guo, and Johnny C. Ho*

Due to the tunable bandgaps, high quantum efficiency, and long carrier diffusion length, perovskites have attracted significant attention as active materials for solar cells, nanoscale lasers, photodetectors, and light-emitting diodes. Herein, laser-induced dual-wavelength emissions from the $CsPbBr_{3x}I_{3(1-x)}$ perovskite alloy microcrystals are reported. Under a 375 nm laser illumination, the micro-photoluminescence (PL) emission spectra of these microcrystals exhibit two emission bands at 570 and 690 nm with gradually increased and decreased PL intensity, respectively. Moreover, the time-dependent emission wavelength of the two emission bands almost has no changes, while the PL intensity of both emission bands shows periodic fluctuations with the on–off switching of excitation light. This dual-wavelength emission phenomenon suggests that phase segregation occurs in these perovskite microcrystals during laser illumination. These results would provide valuable design guidelines for perovskites-based tunable nanophotonic devices and multi-color displays.

1. Introduction

Perovskite materials have attracted tremendous interest due to their high quantum efficiency, low trap-state density, long carrier diffusion length, and tunable bandgaps.[1–11] With these excellent properties, perovskite materials have been widely explored as active materials for solar cells,[12–14] photodetectors,[15,16] and micro/nano-lasers.[17–19] However, organic-inorganic hybrid perovskites, the typical perovskite materials, are mainly restricted by their poor environmental stability, which prohibits their deployment in optoelectronic devices.[20] In contrast, all-inorganic perovskites have significantly improved stability, bringing light into developing high-efficiency optoelectronic devices, including wavelength-tunable emitters, color-full displays, and solid-light sources.[21–23]

Recently, all-inorganic perovskite nanostructures with dual-color or multi-color emissions have been routinely fabricated through anion exchange, ion doping, and phase transition methods, demonstrating their great potential for future optoelectronic devices.[24–27] For instance, $CsPbBr_3$/$CsPbI_3$ heterostructure thin films were realized via a selective anion-exchange process, which was used to investigate dual-color emissions and current rectification behaviors.[25] $CsPbCl_3$/$CsPbI_3$ axial heterostructure nanowires were also examined for dual-wavelength lasing at 425.5 and 687.4 nm, respectively.[28] In addition, many works have as well been reported to evaluate tunable emissions of perovskite materials to understand their mechanism of phase separation,[29–32] which may affect the performance of photoelectronic devices, including solar cells,[33–36] and light-emitting diodes.[37,38] It is generally believed that tunable emissions caused by phase separation in alloy perovskites are owing to the loss of phase stability and separation of different types of halide ions under laser illumination or carrier injection.[30–42] To date, scientists have performed extensive research on halide separation, where many aspects of the process remain controversial in the literature and need further investigation.

Here, we report the synthesis of perovskite alloy microcrystals via a two-step chemical vapor deposition (CVD) method. Scanning electron microscopy (SEM), energy-dispersive X-ray spectroscopy (EDX), and X-ray diffraction (XRD) analysis results suggest that the obtained microcrystals are high-quality with perovskite alloy structures. Dual-wavelength emissions of the microcrystals occur with gradually changed intensity under a continuous wavelength (CW) laser illumination. It is observed that the photoluminescence (PL) emission peak is originally at 570 nm, which is decreased slowly by increasing irradiation time. At the same time, another emission peak starts to appear at 690 nm after introducing laser illumination, and the intensity rises accordingly for the prolonged irradiation. This dual-wavelength emission may be caused by phase segregation in the perovskite alloy structure. This phenomenon of halide ion

Y. Wu, X. Shen, Q. Lv, Q. Yang, D. Liu, Z. Shan, P. Guo
College of Physics and Optoelectronics
Key Laboratory of Advanced Transducers and Intelligent Control System Ministry of Education
Taiyuan University of Technology
Taiyuan 030024, China
E-mail: guopengfei@tyut.edu.cn
P. Guo
Department of Physics
City University of Hong Kong
Kowloon, Hong Kong 999077, China
J. C. Ho
Department of Materials Science and Engineering
City University of Hong Kong
Kowloon, Hong Kong 999077, China
The ORCID identification number(s) for the author(s) of this article can be found under https://doi.org/10.1002/admi.202200680.

DOI: 10.1002/admi.202200680

 © 2022 Wiley-VCH GmbH

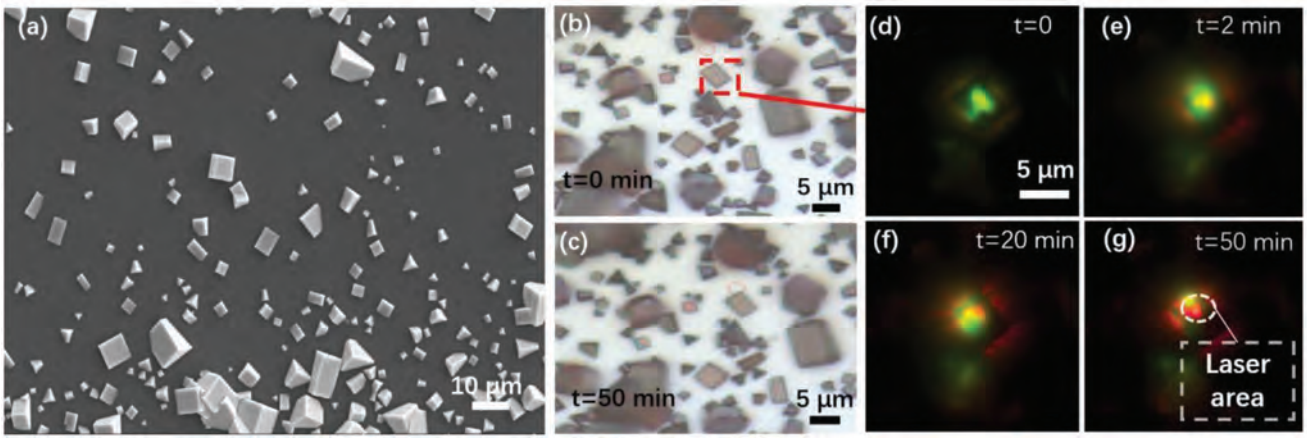

Figure 1. a) Low-resolution top-view SEM image of the perovskite microcrystals. b,c) Optical photographs of the selected perovskite microcrystals before (b) and after (c) laser illumination, respectively. d–g) Dark-field real-color images of a representational microcrystal (red dotted square in b) excited by a 375 nm focused laser illumination from (d) $t = 0$ to (g) $t = 50$ min, respectively.

segregation would always occur in perovskite materials under laser illumination, while the excited state carriers drive the segregation process during laser irradiation.[39–42] These findings give valuable design guidelines for utilizing perovskite materials in phase modulation devices, tunable emitters, and multicolor displays in the future.

2. Results and Discussion

The perovskite microcrystals were synthesized by a two-step CVD method, as depicted in Figure S1 (Supporting Information). Experimental details are shown in the Experiment Section. The SEM image demonstrates that the alloyed perovskite microcrystals are grown on the Si/SiO_2 substrate, with a regular rectangle shape with side lengths of 2–10 μm (**Figure 1**a). Figure 1b,c gives the optical photographs of the perovskite microcrystals before and after laser illumination, respectively, exhibiting nearly the same surface topography. Under a 375 nm laser excitation, the emission colors of a typical microcrystal are gradually changed from green to red with increasing laser illumination time (t = 0–50 min), as illustrated in Figure 1d–g. At first ($t = 0$, Figure 1d), the dark-field PL image of the microcrystals shows a green emission color at 570 nm. As the laser illumination time rises to t = 2 min, red emission starts to appear (Figure 1e,f) from the microcrystal. After laser excitation for 50 min, the emission color of the crystal changes to red (Figure 1g). In order to solve this puzzle, detailed structural characterization and micro-photoluminescence spectroscopy are then performed on these unique alloy perovskite microcrystals.

Figure 2a,b shows the SEM image and optical photograph of the alloyed perovskite microcrystals. They exhibit a square-like structure with side lengths of about 2–10 μm. The XRD pattern of these perovskite structures is displayed in Figure S2 (Supporting Information), where they are indexed to the monoclinic phase. Figure 2c illustrates the EDX analysis of a typical microcrystal before laser illumination as indicated in the panel (a). The atomic ratio of each constituent is measured as Cs:Pb:I:Br = 16:22:12:49. These results are in good agreement with the expected atomic ratio of Cs:Pb:X = 1:1:3 (X = I, Br), indicating that the nanostructures are indeed perovskite alloyed ($CsPbI_{0.6}Br_{2.4}$) structures. The corresponding two-dimensional (2D) elemental mapping of a typical microcrystal is shown in Figure 2d–h. The results reveal the homogeneous atomic distribution throughout the entire microstructure. These findings suggest that the perovskite microcrystals are single crystalline with homogeneous atomic distributions.

To further explore the optical properties of these perovskite microcrystals, the PL spectra and corresponding dark-field emission images are collected by a confocal optical system, as shown in Figure S3 (Supporting Information). To be specific, a 375 nm CW-laser is focused and irradiated onto the microcrystal, while the in-situ PL spectra and corresponding real-color images are recorded for these microcrystals during laser irradiation (**Figure 3**a–f). At the beginning ($t = 0$, Figure 3a), the PL spectrum of a typical microcrystal shows an emission peak at 570 nm with full width at half maximum of about 17 nm at room temperature, suggesting the band-to-band emission occurred under laser excitation. The corresponding dark-field image exhibits a green emission (inset in Figure 3a), which shows agreement with the PL spectrum. When the laser illumination time increases to 20 s, an emission peak at 690 nm emerges and arises gradually along with the illumination time (Figure 3b). After 70 s, red emission appears from the exciting position (Figure 3c), and the PL spectrum simultaneously shows dual-wavelength emission at 570 and 690 nm. As the laser illumination time goes on, the PL intensity at 570 nm decreases, and the 690 nm peak increases gradually without apparent peak shift (Figure 3d–f). At the same time, the emission images of the microcrystals are changed from green to red during laser excitation (t = 0–50 min). It is worth noting that the emission colors are altered in the irradiated regions, indicating that the laser-induced local phase segregation may occur in the irradiated area.

Moreover, it is essential to investigate the laser-induced emission changes of these microcrystals. A series of time-dependent PL spectra are recorded from $t = 0$ to $t = 50$ min, as shown in **Figure 4**. Figure 4a shows the time-dependent 3D PL spectra of

© 2022 Wiley-VCH GmbH

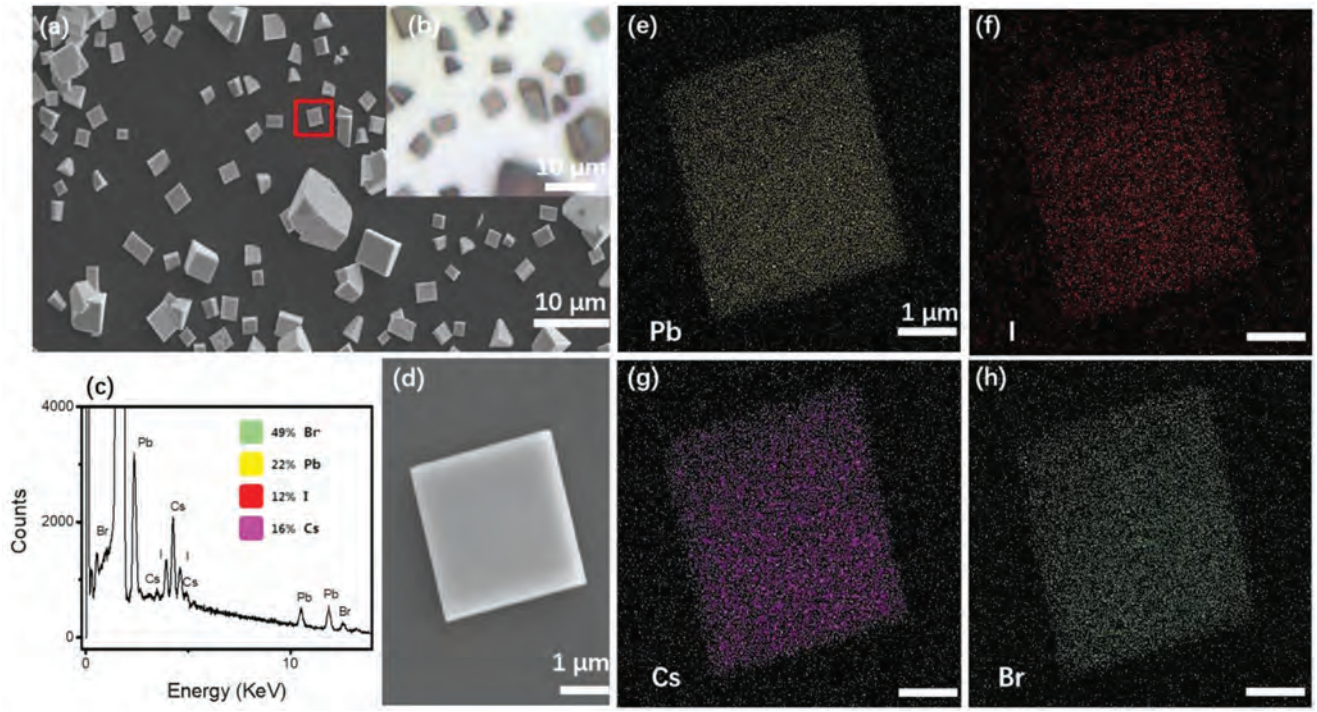

Figure 2. a) SEM image and b) optical photograph of some perovskite alloy microcrystals after laser illumination for 50 min. c) EDX elemental profiles of a perovskite microcrystal as shown in (d). e–h) Corresponding EDX mappings of the typical perovskite alloy microcrystal as indicated in (d).

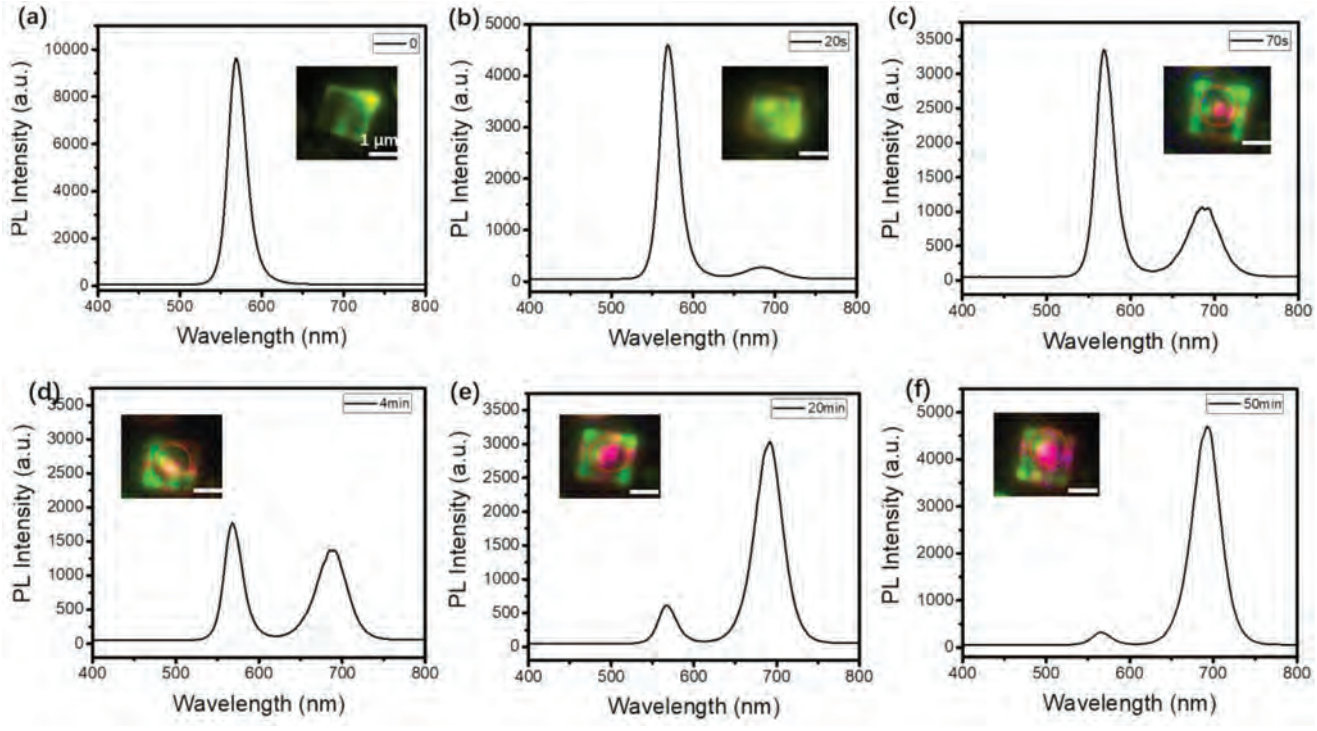

Figure 3. PL spectra and corresponding dark-field real-color images of an individual perovskite alloy microcrystal. a) PL spectrum and real-color image of a typical microcrystal under a focused 375 nm laser illumination at $t = 0$. b–f) PL spectra and corresponding dark-field real-color images of the selected microcrystal under laser illumination time at $t = 20$ s, 70 s, 4, 20, and 50 min, respectively. The scale bar is 1 µm.

© 2022 Wiley-VCH GmbH

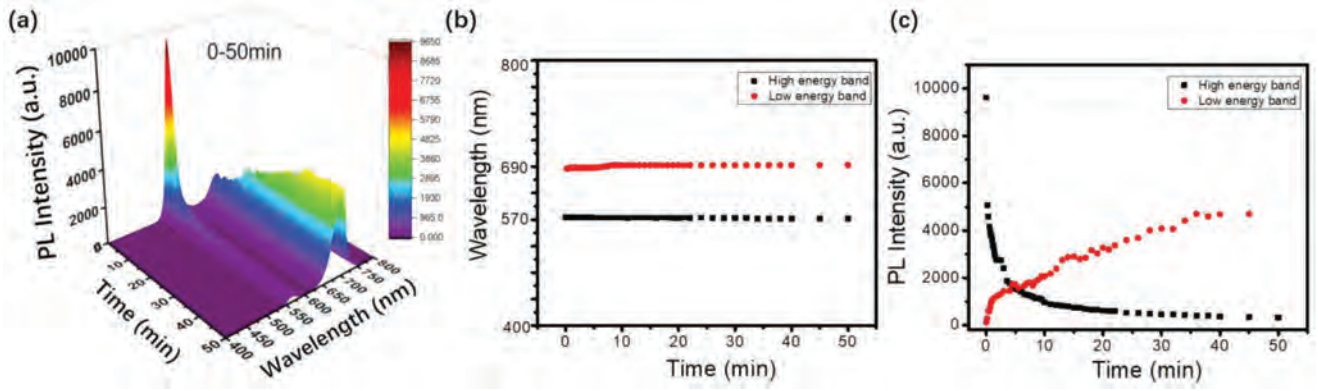

Figure 4. a) 3D evolved PL spectra of a perovskite microcrystal recorded from 0 to 50 min, under a 375 nm laser illumination. b) Time-dependent emission wavelength of the two emission peaks (570 and 690 nm) from $t = 0$ to $t = 50$ min. c) Time-dependent PL intensity of the two peaks at 570 and 690 nm, respectively.

a representative microcrystal under a 375 nm laser illumination at room temperature. The continuously changed PL spectra recorded from 0 to 50 min exhibit the emission changes of the two peaks in Figure 4a. As can be seen, the intensity of the high energy emission band at 570 nm decreases gradually. In comparison, the low energy band at 690 nm rises rapidly and finally tends to be stable. Also, the emission wavelength of the two peaks at 690 and 570 nm have no apparent changes during laser illumination (Figure 4b). Notably, the PL intensity of both emission peaks are changed by the laser illumination time, as shown in Figure 4c. It can be seen that the high energy band decreased rapidly, and the low energy band raised gradually along with the laser irradiation time.

After laser irradiation, the EDX characterizations of the fixed microcrystal are performed again, as shown in Figure S4 (Supporting Information). It is observed that the detected perovskite microcrystal has a uniform morphology with smooth surfaces. In contrast, the elemental distribution of the microcrystal has no significant difference compared to the original crystal. This laser-induced dual-wavelength emission of the perovskite microcrystals may be caused by the formation of lower energy band perovskite inclusions from the higher energy band perovskite, which eventually formed well-mixed perovskite phases under laser illumination.[35–42] It is because the light-induced phase segregation phenomena in mixed halide perovskites were reported, in which photo-excitation induces halide migration and results in lower bandgap iodide-rich domains exhibiting the lower energy band emission.[35,37,39] This phenomenon is different from the dual-wavelength emission in scintillation crystals under a light excitation, which is related to the self-trapping emission at small crystal sizes.[43–47] This spatially inhomogeneous mixed halide perovskite with different band gaps under irradiation may be derived from the phase segregation of perovskites.[40,41] Owing to the relatively long lifetimes and carrier diffusion lengths, under illumination, the photogenerated carriers would occupy a significant volume fraction of the lattice before radiative recombination.[48,49] The carriers have ample opportunities to survey multiple crystallographic domains during diffusion. The carriers can then rapidly thermalize and become trapped upon encountering any I-rich low bandgap region. The change in band structure between an I-rich domain and the uniformly mixed perovskite can also generate an electric field that might further aid in sweeping carriers into the I-rich domain.[50,51] Therefore, under laser illumination for a short time, the PL emission should come from the radiative relaxation of carriers trapped in the I-rich region, consistent with the results of PL measurements as shown in Figure 4c. Moreover, recent transient absorption measurements and investigations support our proposals that phase segregation takes place and that carriers quickly relax into the trap state by showing transient bleaches of both a high-band-gap and low-band-gap phase.[50,52] Thus, all these results may indicate that once excited carriers have driven phase segregation, rapid thermalization of those carriers from the higher-band gap to the new, lower-energy state occurs in a short time.

In addition, to shed light on the mechanism of laser-induced dual-wavelength modulated emission, the measurements with the laser beam modulated on and off are performed, as shown in **Figure 5**. Figure 5a shows the dark-field real-color images of a typical microcrystal under a focused 375 nm laser illumination recorded at a different time from three testing cycles (a1-a4, b1-b4, and c1-c4), respectively. At the beginning ($t = 0$), a laser beam is focused and excited at a representational microcrystal. Four emission images (a1-a4) and corresponding PL spectra (PL_{a1}-PL_{a4} in Figure 5b) are recorded at $t = 10$ s, 540 s, 1080 s, and 1560 s, respectively. As can be seen, the low energy emission band (690 nm) starts to increase with the laser time. After the illumination time of 1560 s, the laser beam is turned off. After 10 min, the laser is turned on again, and the emission images (b1-b4 in Figure 5a) and PL spectra (PL_{b1}-PL_{b4} in Figure 5c) are recorded, which indicates that the emission wavelength is dominated at 690 nm. After 3080 s, the laser is turned on again, while the real-color emission images (c1-c4 in Figure 5a) and PL spectra (PL_{c1}-PL_{c4} in Figure 5d) show little difference with the second cycle ($t = 2160$–2480 s). At the same time, the time-dependent emission wavelength of two emission bands at 570 and 690 nm are shown in Figure 5e. It is observed that both of the emission bands are stable and unchanged. Figure 5f shows the time-dependent PL intensity of the two emission bands with the switch of excitation light. The emission intensity of the high-energy band decreases gradually and tends to be stable under laser excitation. However, the emission

© 2022 Wiley-VCH GmbH

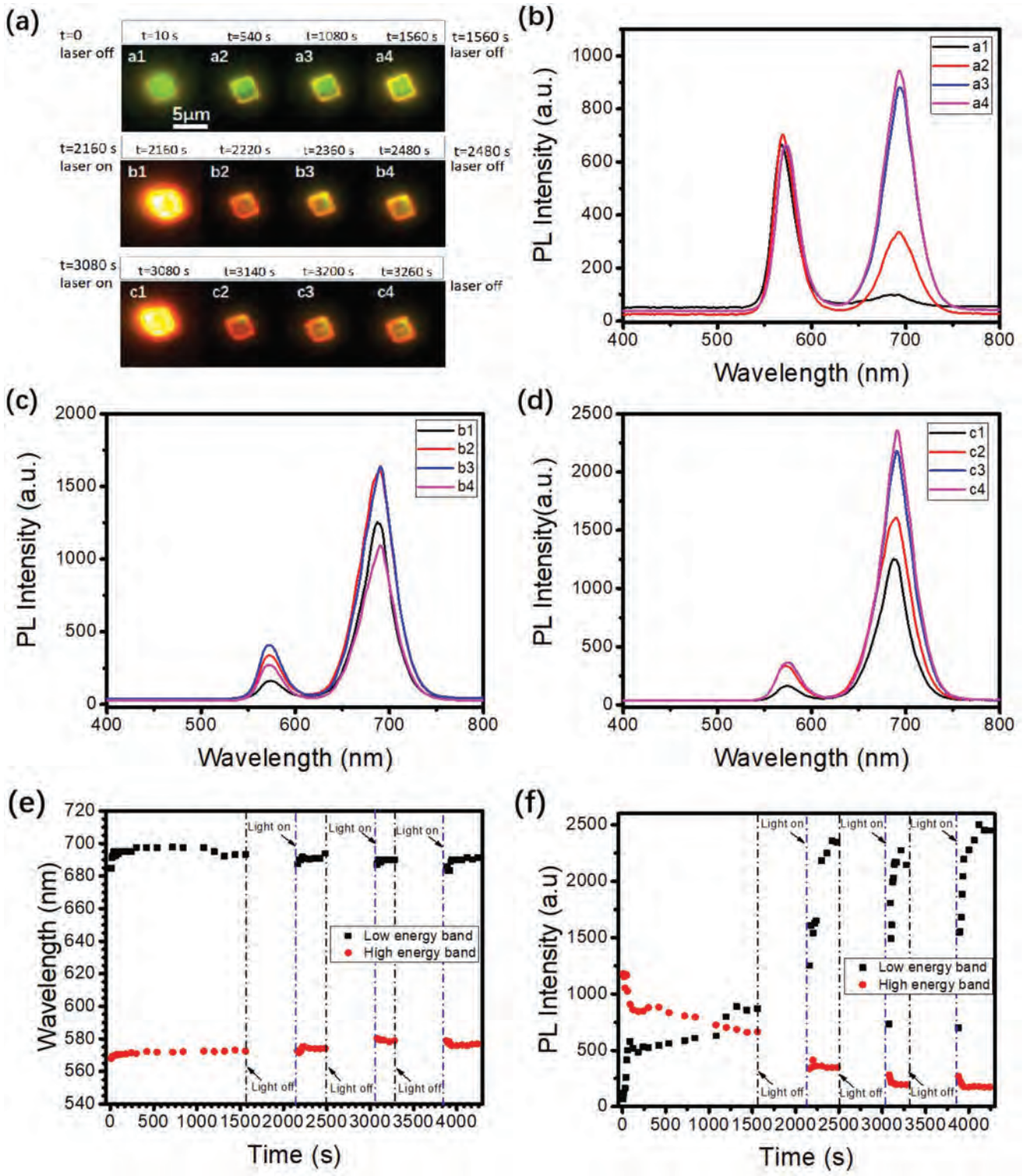

Figure 5. a) Dark-field real-color images of a typical microcrystal under a 375 nm focused laser illumination were recorded at different times from three testing cycles (a1-a4, b1-b4, and c1-c4), respectively. b–d) Corresponding PL spectra of the perovskite microcrystal, which are excited at different times from $t = 0$ s to $t = 3260$ s, respectively. e) Time-dependent emission wavelength of the two emission bands at 570 and 690 nm, respectively. The isolation time is 10 min between light on and off. f) Time-dependent PL intensity of the two emission bands with the on-off switch of excitation light.

intensity of the low-energy band fluctuates periodically with the switch of excitation light. These results indicate that the halide ions segregation phenomenon will not continue once the laser is turned off. It is now accepted that excited state carriers drive the segregation process because halide segregation was observed in the perovskite materials, even in the absence of

© 2022 Wiley-VCH GmbH

light.[40–42] Furthermore, it is considered that the entropy mixing here drives returning to the original state after removing the excitation source.[41,42]

3. Conclusion

In summary, we report a two-step CVD method to synthesize metal halide perovskite microcrystals. The SEM, XRD, and EDX profiles indicate that these microcrystals are single crystalline with side lengths of about 2–10 μm. Under a CW-laser illumination, the PL emission spectra of the microcrystals show dual-wavelength emissions at 570 and 690 nm, which can be continuously changed by the laser illumination time. Moreover, the time-dependent PL intensity of the two emission bands with the switch of excitation light is systematically investigated, which indicates the intensity of the high energy band decreased, and the low energy band increased gradually. This unique emission modulation suggests that the phase segregation may occur during the laser illumination. These interesting findings would have potential applications in multi-color displays and tunable emission devices.

4. Experimental Section

Material Preparation: The perovskite alloy microcrystals were obtained by a two-step CVD method. Firstly, the tube furnace (OTD-1200X) with a long quartz tube (50 mm in diameter and 180 cm in length) was horizontally located at a table, as shown in Figure S1 (Supporting Information). A fine quartz tube (25 mm in diameter and 120 cm in length) was put inside the big tube. Then, a quartz boat (18 mm in length and 8 mm in height) was put with the mixture of $PbBr_2$/CsBr powder (mole ratio = 1:2, Alfa Aesar, 99.9%) in the small quartz tube at the heating area of the furnace. A second quartz boat with the mixture of PbI_2/CsI powder (mole ratio = 1:2, Alfa Aesar, 99.9%) was put inside the small tube and placed away from the heating zone of the furnace before growth. Ar gas was injected into the tube at a flow rate of 80 sccm for 30 min to ensure the removal of ambient air. Meanwhile, the process pressure was pumped down to 3.2 Torr. After that, $CsPbBr_3$ microcrystals were grown first with a pressure of 3.2 Torr and a temperature of 550 °C for 20 min, as shown in Step 1 (Figure S1, Supporting Information). Next, the second boat with PbI_2 and CsI powders were pushed into the furnace in 5 min, while the first boat was pushed out of the furnace in a step-by-step manner. The furnace temperature was kept for 10 min, then cooled to room temperature. The process pressure was maintained at 3.2 Torr throughout the entire growth process.

Optical Characterizations: The PL spectra were obtained by a confocal optical system. A 375 nm excitation laser beam was focused (spot size ≈2 μm) by a microscope objective (Nikon, ×20) and then pumped locally onto the perovskite nanostructures. The far-field optical images were recorded by a charge-coupled device color camera, as shown in Figure S3 (Supporting Information). The PL spectra were recorded by Ocean Optics Spectrometer (Maya Pro2000).

Supporting Information

Supporting Information is available from the Wiley Online Library or from the author.

Acknowledgements

Y.W. and X.S. contributed equally to this work. The authors thank the start-up funding from the Taiyuan University of Technology and Shanxi Basic Research Program Project (No. 20210302123128) for financial support. JCH acknowledges support from the General Research Fund (CityU 11306520) of the Research Grants Council of Hong Kong SAR, China.

Conflict of Interest

The authors declare no conflict of interest.

Data Availability Statement

The data that support the findings of this study are available in the supplementary material of this article.

Keywords

alloy microcrystals, dual-wavelength emissions, laser-induced modulation, lead halide perovskite, nanophotonic

Received: March 25, 2022
Revised: June 22, 2022
Published online: August 29, 2022

[1] X. W. Tong, W. Y. Kong, Y. Y. Wang, J. M. Zhu, L. B. Luo, Z. H. Wang, *ACS Appl. Mater. Interfaces* **2017**, *9*, 18977.
[2] X. Qi, Y. Zhang, Q. Ou, S. T. Ha, C. W. Qiu, H. Zhang, Y. B. Cheng, Q. Xiong, Q. Bao, *Small* **2018**, *14*, 1800682.
[3] A. L. Pan, R. B. Liu, B. S. Zou, *Appl. Phys. Lett.* **2006**, *88*, 173102.
[4] Q. Jing, M. Zhang, X. Huang, X. Ren, P. Wang, Z. Lu, *Nanoscale* **2017**, *9*, 7391.
[5] F. Hao, C. C. Stoumpos, R. P. H. Chang, M. G. Kanatzidis, *J. Am. Chem. Soc.* **2014**, *136*, 8094.
[6] S. T. Ha, R. Su, J. Xing, Q. Zhang, Q. Xiong, *Chem. Sci.* **2017**, *8*, 2522.
[7] M. A. Green, A. Ho-Baillie, H. J. Snaith, *Nat. Photonics* **2014**, *8*, 506.
[8] A. Dutta, R. K. Behera, S. K. Dutta, S. Das Adhikari, N. Pradhan, *J. Phys. Chem. Lett.* **2018**, *9*, 6599.
[9] T. M. Brenner, D. A. Egger, L. Kronik, G. Hodes, D. Cahen, *Nat. Rev. Mater.* **2016**, *1*, 15007.
[10] J. Zhang, Q. Wang, X. Zhang, J. Jiang, Z. Gao, Z. Jin, S. Liu, *RSC Adv.* **2017**, *7*, 36722.
[11] Y. Zhang, J. Du, X. Wu, G. Zhang, Y. Chu, D. Liu, Y. Zhao, Z. Liang, J. Huang, *ACS Appl. Mater. Interfaces* **2015**, *7*, 21634.
[12] N.-G. Park, *Mater. Today* **2015**, *18*, 65.
[13] C. Zuo, H. J. Bolink, H. Han, J. Huang, D. Cahen, L. Ding, *Adv. Sci.* **2016**, *3*, 1500324.
[14] H. Zhou, Q. Chen, G. Li, S. Luo, T.-b. Song, H.-S. Duan, Z. Hong, J. You, Y. Liu, Y. Yang, *Science* **2014**, *345*, 542.
[15] D. Liu, Z. Hu, W. Hu, P. Wangyang, K. Yu, M. Wen, Z. Zu, J. Liu, M. Wang, W. Chen, M. Zhou, X. Tang, Z. Zang, *Mater. Lett.* **2017**, *186*, 243.
[16] S. Chen, C. Teng, M. Zhang, Y. Li, D. Xie, G. Shi, *Adv. Mater.* **2016**, *28*, 5969.
[17] Y. Xu, Q. Chen, C. Zhang, R. Wang, H. Wu, X. Zhang, G. Xing, W. W. Yu, X. Wang, Y. Zhang, M. Xiao, *J. Am. Chem. Soc.* **2016**, *138*, 3761.
[18] S.-T. Ha, C. Shen, J. Zhang, Q. Xiong, *Nat. Photonics* **2016**, *10*, 115.
[19] M. M. Stylianakis, T. Maksudov, A. Panagiotopoulos, G. Kakavelakis, K. Petridis, *Materials* **2019**, *12*, 859.

 © 2022 Wiley-VCH GmbH

[20] J. C. Yu, D. B. Kim, G. Baek, B. R. Lee, E. D. Jung, S. Lee, J. H. Chu, D.-K. Lee, K. J. Choi, S. Cho, M. H. Song, *Adv. Mater.* **2015**, *27*, 3492.
[21] G. Niu, X. Guo, L. Wang, *J. Mater. Chem. A* **2015**, *3*, 8970.
[22] N. A. N. Ouedraogo, Y. Chen, Y. Y. Xiao, Q. Meng, C. B. Han, H. Yan, Y. Zhang, *Nano Energy* **2020**, *67*, 104249.
[23] D. Wang, M. Wright, N. K. Elumalai, A. Uddin, *Sol. Energy Mater. Sol. Cells* **2016**, *147*, 255.
[24] L. Dou, M. Lai, S. K. Christopher, Y. Yang, G. B. Connor, D. Zhang, W. E. Samuel, S. G. Naomi, P. Yang, *Proc. Natl. Acad. Sci.* **2017**, *114*, 7216.
[25] Y. Wang, C. Jia, Z. Fan, Z. Lin, S.-J. Lee, T. L. Atallah, J. R. Caram, Y. Huang, X. Duan, *Nano Lett.* **2021**, *21*, 1454.
[26] Y. Wang, Z. Chen, F. Deschler, X. Sun, T.-M. Lu, E. A. Wertz, J.-M. Hu, J. Shi, *ACS Nano* **2017**, *11*, 3355.
[27] Q. Ba, A. Jana, L. Wang, K. S. Kim, *Adv. Funct. Mater.* **2019**, *29*, 1904768.
[28] P. Guo, D. Liu, X. Shen, Q. Lv, Y. Wu, Q. Yang, P. Li, Y. Hao, J. C. Ho, K. M. Yu, *Nano Energy* **2022**, *92*, 106778.
[29] K. Suchan, A. Merdasa, C. Rehermann, E. L. Unger, I. G. Scheblykin, *J. Lumin.* **2020**, *221*, 117073.
[30] C. G. Bischak, C. L. Hetherington, H. Wu, S. Aloni, D. F. Ogletree, D. T. Limmer, N. S. Ginsberg, *Nano Lett.* **2017**, *17*, 1028.
[31] J. F. Galisteo-López, M. Anaya, M. E. Calvo, H. Míguez, *J. Phys. Chem. Lett.* **2015**, *6*, 2200.
[32] W. Li, M. U. Rothmann, A. Liu, Z. Wang, Y. Zhang, A. R. Pascoe, J. Lu, L. Jiang, Y. Chen, F. Huang, Y. Peng, Q. Bao, J. Etheridge, U. Bach, Y.-B. Cheng, *Adv. Energy Mater.* **2017**, *7*, 1700946.
[33] S. Mahesh, J. M. Ball, R. D. J. Oliver, D. P. McMeekin, P. K. Nayak, M. B. Johnston, H. J. Snaith, *Energy Environ. Sci.* **2020**, *13*, 258.
[34] I. L. Braly, R. J. Stoddard, A. Rajagopal, A. R. Uhl, J. K. Katahara, A. K. Y. Jen, H. W. Hillhouse, *ACS Energy Lett.* **2017**, *2*, 1841.
[35] T. Duong, H. K. Mulmudi, Y. Wu, X. Fu, H. Shen, J. Peng, N. Wu, H. T. Nguyen, D. Macdonald, M. Lockrey, T. P. White, K. Weber, K. Catchpole, *ACS Appl. Mater. Interfaces* **2017**, *9*, 26859.
[36] G. F. Samu, C. Janáky, P. V. Kamat, *ACS Energy Lett.* **2017**, *2*, 1860.
[37] P. Vashishtha, J. E. Halpert, *Chem. Mater.* **2017**, *29*, 5965.
[38] Y. Shynkarenko, M. I. Bodnarchuk, C. Bernasconi, Y. Berezovska, V. Verteletskyi, S. T. Ochsenbein, M. V. Kovalenko, *ACS Energy Lett.* **2019**, *4*, 2703.
[39] T. Elmelund, B. Seger, M. Kuno, P. V. Kamat, *ACS Energy Lett.* **2020**, *5*, 56.
[40] S. J. Yoon, M. Kuno, P. V. Kamat, *ACS Energy Lett.* **2017**, *2*, 1507.
[41] W. Chen, W. Mao, U. Bach, B. Jia, X. Wen, *Small Methods* **2019**, *3*, 1900273.
[42] C. M. Sutter-Fella, Q. P. Ngo, N. Cefarin, K. L. Gardner, N. Tamura, C. V. Stan, W. S. Drisdell, A. Javey, F. M. Toma, I. D. Sharp, *Nano Lett.* **2018**, *18*, 3473.
[43] R. Lin, Q. Guo, Q. Zhu, Y. Zhu, W. Zheng, F. Huang, *Adv. Mater.* **2019**, *31*, 1905079.
[44] R. Lin, Q. Zhu, Q. Guo, Y. Zhu, W. Zheng, F. Huang, *J. Phys. Chem. C* **2020**, *124*, 20469.
[45] Y. Ding, R. Lin, Y. Liang, W. Zheng, L. Chen, X. Ouyang, X. Ouyang, F. Huang, *J. Phys. Chem. Lett.* **2021**, *12*, 7342.
[46] R. Lin, Y. Ding, W. Zheng, M. Jin, L. Chen, X. Ouyang, F. Huang, *Cell Rep. Phys. Sci.* **2021**, *2*, 100437.
[47] X. Ouyang, R. Lin, Y. Ding, Y. Liang, W. Zheng, L. Chen, X. Song, F. Huang, X. Ouyang, *Mater. Chem. Front.* **2021**, *5*, 4739.
[48] D. S. Samuel, E. E. Giles, G. Grancini, C. Menelaou, J. P. A. Marcelo, T. Leijtens, M. H. Laura, A. Petrozza, J. S. Henry, *Science* **2013**, *342*, 341.
[49] G. Xing, N. Mathews, S. Sun, S. Lim Swee, M. Lam Yeng, M. Grätzel, S. Mhaisalkar, C. Sum Tze, *Science* **2013**, *342*, 344.
[50] D. Shi, V. Adinolfi, R. Comin, M. Yuan, E. Alarousu, A. Buin, Y. Chen, S. Hoogland, A. Rothenberger, K. Katsiev, Y. Losovyj, X. Zhang, A. D. Peter, F. Mohammed Omar, H. S. Edward, M. B. Osman, *Science* **2015**, *347*, 519.
[51] D. J. Slotcavage, H. I. Karunadasa, M. D. McGehee, *ACS Energy Lett.* **2016**, *1*, 1199.
[52] S. J. Yoon, S. Draguta, J. S. Manser, O. Sharia, W. F. Schneider, M. Kuno, P. V. Kamat, *ACS Energy Lett.* **2016**, *1*, 290.

© 2022 Wiley-VCH GmbH